On the initiation, propagation and reorientation of simultaneously-induced multiple hydraulic fractures

Kang Duan [1], Chung Yee Kwok [2,*], Qiangyong Zhang[3,*], Junlong Shang[4]

[1] *School of Civil Engineering, Shandong University, Jinan, China*

[2] *Department of Civil Engineering, The University of Hong Kong, Hong Kong*

[3] *Research Centre of Geotechnical and Structural Engineering, Shandong University, Jinan, China*

[4] *School of Civil and Environmental Engineering, Nanyang Technological University, Singapore*

* Corresponding author (Email: fkwok8@hku.hk; qiangyongz@sdu.edu.cn)

Abstract: This study aims to uncover the growth characteristics of simultaneously-induced multiple hydraulic fractures using the discrete element method. We evaluate the influences of in-situ states and operational parameters on the fracture trajectories. Results reveal that reservoir heterogeneity magnifies the stress-shadowing effect and causes severe interactions among fractures. Higher effective stress anisotropy offsets the stress-shadowing effect and force the fractures to propagate in the direction of maximum stress and results in relative long parallel fractures. Increasing the spacing can mitigate the stress-shadowing effect to some degree. Injection rate and fluid viscosity have a less significant influence on the interactions among fractures.

Keywords: hydraulic fracturing, discrete element method, stress-shadowing effect, simultaneous multiple fractures, formation heterogeneity

1 Introduction

Simultaneous multiple fracturing treatment from a horizontal wellbore has been widely used in the oil/gas industry and the enhanced geothermal system to enlarge the stimulated volume of the reservoir. It is a prevalent approach to reduce the operation cost, and to create several hydraulic fractures (HFs) at once [1]. One challenge to effectively use this technique is to generate effective HFs from all perforation clusters. It is generally believed that longer and persistent fractures along the orientation of the maximum stress will lead to an optimal conductivity [2-4]. However, the fracture paths in reality are highly unpredictable.

Analysis of production logs from several basins indicates that about 30% of perforation clusters might not contribute to production [5-7]. Possible reasons are attributed to the fact that the interactions among multiple fractures lead to the preferential growth of some fractures during the treatment. Field analysis results from advanced diagnostic technologies confirm that simultaneous propagation of multiple fractures is often not uniformly developed [6, 8]. In fact, opening of a fracture induces excessive compression (known as the 'stress shadowing') that causes the adjacent fractures to curve away from each other and the appearance of the dominant perforation clusters during simultaneous stimulation of multiple fractures [9-11]. A comprehensive understanding of the stress shadowing effect and the physical processes underlying the growth of simultaneous multiple HFs is essential for the proposing of proper treatments which can minimize the negative effect of stress shadowing and promote more uniform fracture growth.

Several factors including the geological complexity, the uncertainty and spatial variability of reservoir properties contribute to the complication of physical process underling the multiple hydraulic fracturing. Moreover, it is still difficult to measure the geometry of hydraulic fractures directly so far. Limited access to the treated formation makes the interpretation of field monitoring information more difficult and uncertain [12], and thus hinder our understanding towards the mechanisms underlying the propagation and interaction among multiple fractures.

An extensive body of experiments have been designed in the laboratory at reduced-scale to uncover the mechanics of HFs in natural and artificial rocks [13-16]. Although most of the experiments are conducted on the growth of a single HF, they have confirmed the complexity of the physical process involved. For instance, multiple experimental results suggest the hydraulic fractures do not develop symmetrically with respect to the injection hole [13, 17]. Different acoustic emission (AE) sources distribution and breakdown pressure are identified from the treatments with the use of oil, water, supercritical and liquid CO_2 [15, 17]. The interaction between pre-fracture and induced fractures display different modes depending on the approaching angle and differential stress level [18]. Recently, pioneering work has been done to study the initiation of multiple fractures induced by cyclic pumping using cuboid concrete specimens [19]. Notwithstanding these findings, the influences of in-situ and operational parameters deserve a thorough examination to elucidate the mechanisms underlying the fracturing process.

Numerical approaches have been developed to solve the fully coupled problems underlying the growth of hydraulic fractures [20-23], which involve several fields of physical concepts including, elastic deformation, poro-mechanics, fluid mechanics, and fracture mechanics [24]. To model the hydraulic fracturing, coupling of the following three processes should be considered: the mechanical deformation caused by the fluid pressure, fluid flow inside the fracture, and the propagation of fracture. Numerous constitutive equations have been developed to describe each of the physical process and the coupling process among them. Different with the continuum approach, the discontinuous methods can simulate the fracturing process of rocks under different stress conditions at multi-scales with mathematically simple contact relations [25-29].

Based on the pipe-network coupling algorithm, Discrete Element Method (DEM) has been widely adopted in the simulation of hydro-mechanical responses of rock materials. Both quantitative and qualitative comparisons with analytical, numerical, experimental or field results have been conducted to confirm the validity of the numerical approach to reproduce the fluid flow behaviors [30-32], the hydraulic fracturing [33-36] and the injection induced seismicity [37, 38]. Multi-branched growth of fractures have also been investigated by DEM simulation, with emphasis on increasing the hydraulic fracture complexity [39, 40]. Nevertheless, more efforts are still necessary to systematically evaluate the influences of various factors on the stress shadowing effect and mutual interactions among multiple fractures. The innovative academic contributions of this study lie in the comprehensive parametric studies and the acquisition of critical information regarding local rock deformation, pressure alteration, fracture interaction and reorientation.

We investigate the initiation, propagation and reorientation of simultaneously-induced multiple hydraulic fractures using the fully-coupled two-dimensional particle flow code (PFC2D) [41]. Injection rate is maintained constant during the whole fracturing process to perform a fair comparison between the stress shadowing effect and the influence of various parameters. Although this scenario deviates from the reality, where the constant fluid influx into the wellbore is dynamically partitioned to each fracture so that the wellbore pressure is the same throughout the array, we simplify the scenario into the mutual interaction among multiple fractures since the fracturing path in reality can be extremely complex and random. We first validate the numerical model by comparing the stress alteration caused by the opening of a fracture with the model. Thereafter, we perform a set of comparative studies to assess the influences of the in-situ conditions (maximum horizontal stress, initial pore pressure and reservoir heterogeneity) and operational parameters (intervals, injection rate and fluid viscosity) on the fracture propagation trajectories.

2 Setup of the DEM model

Genesis of the DEM model follows the procedures recommended by Ref [25], which consists of 4 steps: compact initial assembly; install specified isotropic stress; reduce the number of ‘floating’ particles; install parallel bonds, and remove from material vessel. As illustrated in Fig 1a, the 200 m × 200 m square-shaped model consists of 11,710 particles and 23,529 parallel bonds. The particle size follows a uniform distribution (R_{max}/R_{min}=1.66) with an average diameter of 2.0 m. Model generated in this way has a coordination number of 4.09. Note that the particle in the model is a simple way to discretize the space and thus cannot be treated as a single block in the reservoir. Selection of the particle size and size distribution is optimized by considering both the representativeness of the model and the computational effectiveness. In this section, we provide brief introductions to the two key components of the model, i.e., the bonded particle model representing the rock formation and the fluid flow model simulating the hydro-mechanical coupling responses. After that, we provide detailed information about the boundary conditions and the selection of micro-parameters.

2.1 Bonded particle model (BPM)

In the DEM model, rock formation is represented by an assembly of discs (yellow circles in Fig 1b) bonded at their contacts (red lines in Fig 1b), known as the bonded particle model [25]. Interactions between the contacting two particles are described by the force-displacement relationship, i.e., the linear contact model, while the movements of the particles are governed by the Newton’s second law. Location, force and displacement of the particles are updated upon a time-stepping algorithm. The bond may break once the stress acting on it exceeds the strength, in terms of tensile or shear component. Each bond breakage is idealized to be a crack which can be classified into the tensile or shear mode according to the failure mechanism. In this way, initiation, propagation and interaction of fractures can be explicitly simulated.

2.2 Fluid flow model

As illustrated in Fig 1b, a set of domains can be identified in the DEM model by drawing all contacts between particles (red lines). Each close region is assumed to be a reservoir (Blue dots enclosed by red lines). These reservoirs are connected by pipes. Fluid flow is simulated in the 2D DEM model by assuming that each contact has an initial aperture. As illustrated in Fig 1c, with the assumption of laminar flow between parallel plates, the volumetric flow rate through the pipe can be calculated as:

$$Q = \frac{w^3 \Delta P}{12L} \tag{1}$$

where w is the aperture of pipe, ΔP is the pressure difference crossing the pipe and L is the length of the pipe (see Fig 1c), which is assumed to be the averaged particle diameter.

A virtual aperture is assumed at the contact to ensure fluid flow can occur crossing two particles in touch (See Fig 1c). We assume this aperture never decreases to zero. The relation between the aperture (w) and the compressive contact force (F) is defined as:

$$w = \frac{w_0 F_0}{F + F_0} \tag{2}$$

where F_0 is the force when the aperture decreases to half of the residual aperture (w_0).

During the fluid flow calculation, each domain receives a certain volume of fluid from its surrounding pipes. Given the total volume ($\sum Q$) of fluid during one time step (Δt), the update of fluid pressure can be calculated as:

$$\Delta P = \frac{K_f}{V_d}(\Sigma Q \Delta t - \Delta V_d) \tag{3}$$

where K_f is the fluid modulus and V_d is the volume of the domain.

Validity of the fluid flow model to simulate the fully coupled hydro-mechanical responses in rock formation have been extensively confirmed in terms of the initiation and subsequent growth of hydraulic fracture from a single hole [33, 35], the interaction with pre-existing fracture [42], injection induced seismicity [38, 42], fault reactivation [37], permeability alternation [31] and stress alteration [2, 34]. We apply this same algorithm into the modeling of simultaneous multiple hydraulic fracturing.

2.3 Boundary condition

We model the reservoir located at an average depth of 3449-3550 m. To represent the typical stress and operational conditions in this site, the following parameters are determined to define the initial state of the model: the vertical stress σ_V=82.74 MPa, the maximum principal horizontal stress σ_{Hmax}=70.26 MPa, and the initial pore pressure P_0=59.32 MPa. The formation is assumed to be isotropic with the aim to isolate the influence of stress shadowing from the effect of sedimentary beddings and pre-existing fractures.

Prior to the injection of fluid, we apply the initial stress states to the model and then saturate the formation with the initial pore pressure. The injection points locate along a horizontal well in the center of the simulated reservoir. The outside model boundary is fixed and impermeable. The size of the wellbore is assumed to be negligible with respect to the size of the fracture, and thus the wellbore is represented by an injection point within a domain in the simulation. We maintain the in-situ stresses constant during the subsequent saturation and injection stages by adjusting the location of boundary walls through the servo control mechanism.

2.4 Determination of the micro-parameters

The micro mechanical parameters of the DEM model listed in Table 1 are calibrated to match the uniaxial compressive strength, the Young's modulus and the Poisson's ratio of the Haynesville Shale [43, 44], which can be found in Table 2. These mechanical properties are obtained from the laboratory tests on brittle Haynesville shale at depth of 3448.8 to 3450.3 m. To do the calibration, we perform a set of virtual uniaxial compressive tests on the DEM sample with the size of 80×160 m. There are roughly 40×80 particles across the sample with the particle size adopted in this study. This meets the limit recommended by the International Society for Rock Mechanics, which requires that the number of grains cross the minimum boundary should be more than 20 in regard to its largest mineral grain size [45].

The target formation is saturated with water under in-situ conditions and intact rock has relatively low in-situ permeability. The equilibrium permeability measured from fluid flow test on the DEM model with scale of 40×40m under the same in-situ conditions is 5.5×10^{-12} m/s. Although the initial pore pressure is present in the model, it is assumed that most of the fluid flow occurs in the hydraulically induced fracture. These assumptions are reasonable and have little, if any, effect on model predictions. Considering the time scale of fluid transport along the open fractures and the relative small aperture of contacts compared with the fractures, leak-off into the matrix due to the permeability is negligible.

3 Validation of the DEM model

We first model the growth of a single fracture stimulated at the formation center and examine the stress alternation induced by the fracture opening with an analytical solution from reference [46]. Setup of the DEM model and boundary condition for the simulation are summarized in Table 3.

3.1 Growth of a single hydraulic fracture

We perform injection treatment at point (0, 0) with a constant rate of 2.12×10^{-5} m^3/s. Note that the injection rate adopted in this study cannot be directly related to the actual values due to the 2D nature of the model [33]. In practice, we choose a rate high enough to induce fracturing but low enough to maintain stability. The well pressure history in Fig 2 follows the typical responses obtained from hydraulic fracturing tests [17, 47], namely, the well pressure increases gradually till a maximum value, known as the breakdown pressure (P_b=176.4 MPa), accompanied by the initiation of fracture. Subsequently, the well pressure drops in a zig-zag pattern, and ultimately approaches to a constant value. The number of cracks increases at an approximately linear rate over time. After the opening of the first crack, slope of the pressure curve at the secondary increasing stages (e.g., from Point B to C) gradually decreases, indicating that the stress needed for the formation of new cracks decreases with the longer fracture. According to Eq. (4)[48], the length of a fracture (a) is inversely proportional to the stress (σ) required to induce bond breakage as fracture toughness (K_{I}) is an intrinsic property of a rock and is a constant.

$$K_I = C(\phi)\sigma\sqrt{\pi a} \tag{4}$$

where $C(\phi)$ is a geometrical factor. This factor is a function of the ratio between crack length and sample width (known as ϕ) and can be calculated from the following equation:

$$C(\phi) = \left[\sec\left(\frac{\pi\phi}{2}\right)\right]^{1/2} \left(1 - 0.025\phi^2 + 0.06\phi^4\right) \tag{5}$$

During the whole fracturing process, all cracks form in terms of tensile failure, which is in line with the linear elastic fracture mechanics. Tempo-spatial evolution of the cracks in Fig 3 illustrates that the single HF propagates vertically as dictated by the initial stress state. However, rather than the systematic growth path predicted by ideal continuum models, the geometry of a single fracture is asymmetric with respect to the injection point. The fracture propagates either upward or downward, depending on the relative resistance at the two fracture tips.

Fig 4 displays the magnitude of fluid pressure along the fracture at various stages. Overall, the pressure drops with the growth of fracture. The pressure is not necessarily uniform along the fracture. Soon after the formation of new cracks (Point B in Fig 2), the pore pressure at the newly-appeared fracture tip is much lower than those close to the injection point. At the stages ahead the formation of new cracks (Point A and C in Fig 2), the pore pressure stays almost constant along the whole fracture after a certain period of fluid diffusion.

3.2 Comparison with the analytical solution

We install a set of measurement circles with a diameter of 10 m (see Fig 5a) to monitor the stress states within the model. Spacing between the adjacent circles equals to 5 m. This diameter is selected considering both the representativeness of specific point and the accuracy of the measured stress. We measure the interior stresses (σ_{xx}, σ_{yy} and σ_{xy}) after the application of in-situ stress ($\sigma_{H\max}$ and σ_V) and after the formation is fully saturated. The effective horizontal stress ($\sigma_{xx}^{'}$) can be calculated by:

$$\sigma_{xx}^{'} = \sigma_{xx} - P_0 \tag{6}$$

The horizontal stress in Fig 5b fluctuates around the applied horizontal in-situ stress ($\sigma_{H\max}$ =70.26 MPa). The degree of fluctuation becomes less significant after the formation is fully saturated (See Fig 5c), implying that presence of pore pressure leads to the adjustment of particle location and the redistribution of contact forces towards a more uniform mode.

Sneddon [46] developed the solutions to calculate the stress state in the interior of an infinite 'two-dimensional; elastic medium' induced by the opening of an internal fracture under the action of a uniform liquid pressure (p_0) inside as the only load. As illustrated in Fig 6, the components of stress (σ_x, σ_y and τ_{xy}) at any point in the vicinity of the fracture (from $x=-c$ to $x=c$) are given by:

$$\frac{1}{2}(\sigma_x + \sigma_y) = p_0\left(\frac{r}{r_1^{\frac{1}{2}} r_2^{\frac{1}{2}}}\cos(\theta - \frac{1}{2}\theta_1 - \frac{1}{2}\theta_2) - 1\right) \tag{7}$$

$$\frac{1}{2}(\sigma_y - \sigma_x) = p_0 \frac{r\sin\theta}{c}\left(\frac{c^2}{r_1 r_2}\right)^{\frac{3}{2}} \sin\frac{3}{2}(\theta_1 + \theta_2) \tag{8}$$

$$\tau_{xy} = p_0 \frac{r\sin\theta}{c}\left(\frac{c^2}{r_1 r_2}\right)^{\frac{3}{2}} \cos\frac{3}{2}(\theta_1 + \theta_2) \tag{9}$$

For the maximum shear stress:

$$\tau = \mathrm{p}_0 \frac{r\sin\theta}{c}\left(\frac{c^2}{r_1 r_2}\right)^{\frac{3}{2}} \tag{10}$$

We select three stages (i.e., Stage A, C and D in Fig 2 and Fig 3) to do the comparison as the fluid pressure at these stages is uniformly distributed and thus meets the prerequisites of the theoretical model. States of the fracture are provided in Table 4. Length of the fracture (L) is estimated from the coordination of the upper and lower tips ((x_{up}, y_{up}) and (x_{low}, y_{low})), by assuming it to be linear and continuous:

$$L = \sqrt{\left(y_{up} - y_{low}\right)^2 + \left(x_{up} - x_{low}\right)^2} \tag{11}$$

Fig 7 compares the geometry of the fracture and the contours of σ_{xx}' obtained numerically and theoretically. Negative stress indicates that the corresponding site is under compression. General well agreement exists between the numerical and theoretical results in sense of the stress state with the growth of fracture. The fracturing-induced stress alterations appear in certain areas of the model. Specifically, opening of HF exerts horizontal compressive stress perpendicular to the fracture trajectory. The degree of alternation declines with distance from the fracture. Tensile stress (positive magnitude in Fig 7b and 7c) concentrates ahead of the fracture tips. Difference exists between the numerical and theoretical results in terms of stress magnitude close to the fracture since the measured stresses are an averaged state of certain number of particles, which cannot reflect the sharp transition close to the fracture interface and the tips.

4. Simultaneous multiple hydraulic fracturing

We first carry out individual fracturing treatment at the four points spaced with 17 m (see Fig 1a), using the same injection rate with the single hydraulic fracturing test. The well pressure histories in Fig 8a present the similar trend with the single HF test (Fig 2). However, slope of the curve varies from case to case due to the non-uniform volume of domains representing the injection points and the number of pipes surrounding each domain. Under the same injection rate, smaller domain leads to a higher well pressure after the same time. Moreover, the breakdown pressure varies from 210.1 to 336.4 MPa, depending on the local tensile strength of the bond and the local force distribution. The values of break down pressure from simulation are much higher than the value commonly encountered in the experimental and field treatments. Possible reasons will be discussed in Section 5. The difference among well pressures becomes smaller with the ongoing of test. Ultimately, all pressures approach to a same magnitude. In Fig 8b, fracture geometry shows that all the four fractures propagate vertically, with the aperture gradually decreasing from the injection point to the tips. However, the fracture trajectory is site-dependent. Fractures A and D are almost symmetric with respect to the injection points while fracture C only propagates downward. This discrepancy is caused by the nonuniformity of rock properties. During the fracturing process, competition exists between the two fracture fronts, depending on the local contact force and local bond strength. Consequently, the fracture propagates along the path with least resistance.

4.1 The reference case

For comparison purpose, we simultaneously inject fluid at the four points with the same setup of the individual treatment case (Fig 8). All well pressure histories (Fig 9) follow the similar trend with the single HF discussed previously. The well pressures also approach to a same magnitude with the ongoing of fracturing. Breakdown pressures obtained from the simultaneous injection test are close to those obtained from the individual injection test (see Fig 10a). This can be explained by the fact that the perturbation of local contact force around the injection points are negligible at the breakdown pressure stage, as confirmed by the force network in Fig 10b and Fig 10c.

Fig 11 and Fig 12 illustrate the growth of fractures and the corresponding contours of $\sigma_{xx}^{'}$. Different with the individual case, stress-shadowing influences the development of multiple fractures. Initiation of early fractures (A and D) alter the magnitudes and orientations of the local principle stress (see Fig 12 when t_{inj}=1323 and 1639s), and hence affect the propagation direction of the late fractures (B and C in Fig 11 when t_{inj}=2347 and 3212s). The interaction between fractures also affects the growth of early fractures, e.g., propagation of fracture D starts to approach the outer of formation from t_{inj}=2347 to 4229 s. When the fracture branches grow in the area far from the existing fractures where stress shadow effect is less pronounced, they turn back toward the direction of the far-field maximum in situ stress (fractures B and D after 4229 s). The lower tips of fracture B and D are suppressed by compression stress induced by facture A and C. On the contrary, the upper tips of A and C fall in the region of stress shadow of facture B and D and are suppressed. As a result, alternative upward and downward fractures appear.

This scenario is regarded as the reference case. In the subsequent two sections, we systematically change the in-situ states (maximum horizontal stress, initial pore pressure and formation heterogeneity) and the operation parameters (injection point spacing, injection rate and fluid viscosity) and evaluate the influence these factors on the characteristics of multiple fractures. In these results, we mainly focus on the geometry of the fractures at the last stage of stimulation.

4.2 Influences of in situ conditions

To describe the in situ stress deviator, the anisotropy ratio of effective stress (α) is defined as:

$$\alpha = \frac{\sigma_V^{'}}{\sigma_{H\max}^{'}} = \frac{\sigma_V - P_0}{\sigma_{H\max} - P_0} \tag{12}$$

where $\sigma_V^{'}$ and $\sigma_H^{'}$ represent the effective vertical stress and the maximum effective horizontal stress, respectively. We conduct hydraulic fracturing tests on the same formation with the reference case but varying the magnitude of the vertical stress, the maximum horizontal stress and the initial pore pressure. Details about the tests are summarized in Table 5.

For the case with larger effective stress deviator (α =4.12), all fractures propagate approximately along the maximum stress direction (Fig 13a and 13c). The growth paths of fractures are almost consistent despite the short inclined segments in fracture B soon after the fracture initiation in Fig 13a caused by stress shadowing. After a certain height, when fracture B overcome the stress shadowing region, it grows upward along the in-situ stress direction again. For the case with lower stress deviator (α =1.49), the influence of stress shadowing is more significant (see Fig 13b and 13d). Fracture A and D surpass others and dominate the propagation. The propagation of two inner fractures (B and C) are severely suspended due to stress interaction with outer fractures at the very beginning. Especially, fracture C grows in the longitude direction due to locally altered stress orientation. The simulation results confirm that fractures in the middle region have smaller aperture because of the increased compressive stresses resulting from other fractures [49]. Maximum fracture aperture appears at the segments just exceeding the region of stress shadowing.

Another parameter contributing to the effective differential stress is the initial pore pressure. We carry two simulations with P_0=55 and 65 MPa, respectively. The case with lower pore pressure leads to smaller effective stress anisotropy (α =1.82), where the stress shadowing influence is more significant. In Fig 14a, fractures generated in the altered stress field (fracture C and the initial segment of fracture B) are shorter and narrower with orientation deviating significantly from the in-situ maximum stress orientation. Fracture A, B and C combine to one major fracture ultimately. The growth of fracture D is obviously suppressed with a comparative small fracture width. There is limited fracture divergence when P_0=65 MPa, because the larger stress anisotropy offsets the effect of fracture turning due to the stress shadow and forces the fracture to go in the direction of maximum stress. Nevertheless, the growth of the two inner fractures (B and C) are suppressed by the two outer ones acting as the dominant fractures (See Fig 14b).

We mimic the texture heterogeneity of rock formation by generating samples with particle size distribution of R_{max}/R_{min}=1.4, 1.66, 1.8 and 2.0, respectively. For each distribution, three packing modes are generated by changing the random number. Simulation results show significant difference between the four cases (see Fig 15). In general, the narrower particle size distribution results in a formation with more uniform properties, in which the parallel fractures can propagate along the maximum principle stress direction for a relative long distance (Fig 15a). Conversely, wider particle size distribution leads to a more heterogeneous fabric, non-uniform force network and thus the concentration of low and high forces. As illustrated in Fig 15c and 15d, heterogeneous rock properties cause the localization of hydraulic fractures and magnify the stress shadowing effect. Fracturing is affected by the local stress in the region within the outer fractures where fractures around becomes inclined and propagate towards the longest one. For the case with largest particle size distribution (Fig 15d), even the longest fracture propagates in an inclined path, rather than the far-field stress dominated vertical direction. Therefore, assumption of radial symmetric fracture growth may only work for the ideal isotropic media while ignoring the formation heterogeneity may underestimate the stress shadowing effect.

4.3 Influence of operational parameters

Since most of the in-situ states are intrinsic for a specific reservoir, we test the possibility of mitigating the stress shadowing effect by changing the injection scheme.

We perform another two injection tests at four points evenly spaced with D=10 m and 20 m, respectively. As compared in Fig 16, increasing the spacing between the injection points can potentially decease the level of interaction between the HFs. The most obvious interactions appear in the model with the minimum spacing (Fig 16a), in which altered local stress orientation cause fracture B propagating horizontally towards A and combining into one major fracture after a short time. Ultimately, two prominent fractures dominate the growth with fracture A propagating upward and fracture C propagating downward. Larger spacing may lead to relative longer fractures with parallel patterns (see Fig 16b and c) but still stress shadowing influence can be identified from the inclined segments within the interaction regions.

With a fixed spacing of 17m, we evaluate the influence of injection rate by conducting hydraulic fracturing with the rate of 0.25, 0.5, 2.0, and 4.0 times of the reference case, respectively. Fig 17 compares the ultimate fracturing patterns. Compared with the in-situ states and the spacing, injection rate has a relative minor influence on the final fracture path. Although the injection time varies, fractures in all the four cases propagate following the same path. Stress shadowing effect forces fracture B propagates away from fracture A at the initial injection phase. Once fracture B overcomes the stress shadowing region, it turns back to propagate upward again. The final fracturing is dominated by two fractures propagate downward (fracture A and C) and two propagate upward (fracture B and D).

We also evaluate the influence of injection fluid viscosity by performing hydraulic fracturing tests with μ =0.0002, 0.0005, 0.005 and 0.02 Pa.s. Generally, fluid viscosity does not influence the trajectory of the fractures much (Fig 18), which is in line with the influence of injection rate. Interaction between nearby fractures exists in a short range, in the form of inclined sections in fracture A, B and D close to the injection points. Once the fracture exceeds its neighboring fractures, stress shadow effect is less pronounced, and the fracture turns back toward the direction of the far-field maximum in-situ stress.

5. Discussions

The breakdown pressures in all cases significantly overestimate the pumping pressure during an actual hydraulic fracturing operation. This pressure corresponds to the pressure in the injection domain when the first bond breaks and depends on the concentration of local contact force, the tensile strength of a single bond, the unrealistic injection rate and the domain volume. Therefore, the breakdown pressure in the DEM model deviates from the physical cases. During the fracture propagation, the well pressure still overestimates the realistic magnitude. Possible reasons include the much higher fracture toughness of the bonded particle model as a consequence of the selected large particle size [25], the implementation of the solid-fluid interaction and inherent issue resulting from the assumption of a discretization in blocks. We make an engineering decision to use a model with high toughness in order to obtain results with practical run time. Our previous study has proved the capacity of flat-jointed model in reproducing both the tensile strength and confinement dependent compressive strength of brittle rocks [50]. Inserting the fluid-flow algorithm into the flat-jointed contact model provides a promising approach to quantitatively capture the fracturing toughness and hydraulic fracturing pressure [51].

During the injection treatment, fracturing occurs when the effective stress exceeds the tensile resistance. Breakdown pressure for the formation with low permeability can be estimated using [52, 53]:

$$P_b = T + 3\sigma_{H\max} - \sigma_V - P_0 \tag{13}$$

where T represents the tensile resistance of the rock formation.

We conduct seven sets of virtual direct tensile tests on the DEM samples with the width ranging from 6 m to 60 m and the height/width ratio fixed as 2.0. For each set, we change the random number and generate 6 samples with different packing. Corresponding tensile strengths are summarized in Fig

19 together with the tensile strength of a single bond. With the increase of the sample size, the tensile strength dramatically drops from the bond strength and then gradually approaches to a constant value around 15 MPa. Taking the tensile strength of a single bond into Eq. 13, we can get the breakdown pressure to be around 117.7 MPa, which is much lower than those presented in Fig 10a. This is caused by the concentration of local contact force. At the subsequent breakdown stages (Point A and C in Fig 2), the equivalent tensile strength approaches ~15 MPa. The breakdown pressure calculated from this tensile strength equals to 83.72 MPa. This magnitude agrees well with the well pressure range between the formation of initial fracture and the propagation stage (see Fig 8), confirming that the simulation results are self-consistent although they overestimate the realistic fracture toughness and well pressure.

As acknowledged in Section 1, we simultaneously inject fluid into the domains with the same rate, resembling the case where fluid is uniformly divided into each fracture. This scenario deviates from the reality, where the constant fluid influx into the wellbore is dynamically partitioned to each fracture so that the wellbore pressure is the same throughout the array. Fracture geometry has been confirmed to be dependent on not only the stress-shadow effect but also the dynamic partitioning of flow rate [1, 5]. Future study is necessary to mimic the nonuniform development of multiple fractures induced by the uneven partitioning of flow rate into each fracture, depending on the flow resistance from fractures by assuming that a uniform pressure exists at all injection points.

According to the theoretical analyses from Detournay [20, 54], two dissipative processes exist during fluid-driven fracturing process, i.e., fracturing of the rock (toughness) and dissipation in the fracturing fluid (viscosity). In the viscosity-dominated regime, the energy expended in the creation of new fracture surfaces is small compared to the energy dissipated in viscous flow, while in the toughness-dominated regime, the viscous dissipation is small compared to the energy dissipated at the crack tip. The conclusion of independence from injection rate and viscosity is assured because the large toughness will have driven the system into a toughness dominate regime. Therefore, the simulation results regarding the influence of injection rate and fluid viscosity are valid under the specific rock properties considered herein. In other words, the results are not universal for other rock with different property. It is necessary to quantitatively capture the tensile strength (i.e., fracture toughness) of the specific rock type and verify if it belongs to the regime where fluid flow is more important in the future study. Orthogonal experimental design considering the influence of fracture toughness and fluid flow parameters is also worth conducting to assess the transition of hydraulic fracturing regimes.

6 Conclusions

We conduct a suite of DEM simulations to investigate the stress-shadowing effect and the growth characteristics of simultaneously-induced multiple fractures under the influences of different factors including the in-situ states and the operational parameters.

Comparison between the theoretical model and simulation results from a single hydraulic fracture confirms the validity of the DEM model to reproduce the fracturing-induced stress alteration. A single hydraulic fracture propagates along the path with least resistance and ultimately leads to the trajectory parallel with the orientation of maximum far field stress but asymmetric with respect to the injection point due to the non-uniformity of formation properties.

Simulation results reveal that the in-situ states play a more dominant role on the interactions among multiple hydraulic fractures. Stress shadowing effect suppress some HFs by the compressive stresses exerted on them by neighboring HFs. Interactions among multiple fractures lead to the appearance of some dominant fractures, propagating either upward or downward. The stress-shadowing effect diminishes with higher effective stress anisotropy, depending on the in-situ stress difference and the initial pore pressure. Non-uniformity of formation properties magnifies the stress shadowing effect and causes the severe interactions among fractures. Increasing the spacing between injection points may mitigate the interactions to a certain degree while changing injection rate and fluid viscosity has a relative minor influence on the stress shadowing and interaction among multiple fractures.

Acknowledgement

Financial supports from the Natural Key Research Development Project of China (No. 2016YFC0401804), the Taishan Scholars Project Foundation of Shandong Province, and the Natural Science Foundation Project of China (NO:41772282) are appreciated.

Reference

[1] Wu K, Olson JE. Mechanisms of simultaneous hydraulic-fracture propagation from multiple perforation clusters in horizontal wells. SPE-163860-PA 2016;21(03):1,000-1,8.

[2] Papachristos E, Scholtès L, Donzé FV, Chareyre B. Intensity and volumetric characterizations of hydraulically driven fractures by hydro-mechanical simulations. Int J Rock Mech Min 2017;93(163-78.

[3] Yoon J, Zimmermann G, Zang A. Numerical Investigation on Stress Shadowing in Fluid Injection-Induced Fracture Propagation in Naturally Fractured Geothermal Reservoirs. Rock Mech Rock Eng 2015;48(4):1439-54.

[4] Yoon JS, Zimmermann G, Zang A. Discrete element modeling of cyclic rate fluid injection at multiple locations in naturally fractured reservoirs. Int J Rock Mech Min 2015;74(0):15-23.

[5] Lecampion B, Desroches J. Simultaneous initiation and growth of multiple radial hydraulic fractures from a horizontal wellbore. Journal of the Mechanics and Physics of Solids 2015;82(235-58.

[6] Miller CK, Waters GA, Rylander EI. Evaluation of production log data from horizontal wells drilled in organic shales. North American Unconventional Gas Conference and Exhibition: Society of Petroleum Engineers, 2011.

[7] Spain DR, Gil IR, Sebastian HM, Smith P, Wampler J, Cadwallader S, et al. Geo-Engineered completion optimization: An integrated, multi-disciplinary approach to improve stimulation efficiency in unconventional shale reservoirs. SPE Middle East Unconventional Resources Conference and Exhibition: Society of Petroleum Engineers, 2015.

[8] Sookprasong P, Gill CC, Hurt RS. Lessons Learned from DAS and DTS in Multicluster, Multistage Horizontal Well Fracturing: Interpretation of Hydraulic Fracture Initiation and Propagation through Diagnostics. IADC/SPE Asia Pacific Drilling Technology Conference: Society of Petroleum Engineers, 2014.

[9] Peirce A, Bunger A. Interference fracturing: nonuniform distributions of perforation clusters that promote simultaneous growth of multiple hydraulic fractures. SPE-163860-PA 2015;20(02):384-95.

[10] Nagel NB, Sanchez-Nagel M. Stress shadowing and microseismic events: A numerical evaluation. SPE Annual Technical Conference and Exhibition: Society of Petroleum Engineers, 2011.

[11] Wu R, Kresse O, Weng X, Cohen C-E, Gu H. Modeling of interaction of hydraulic fractures in complex fracture networks. SPE Hydraulic Fracturing Technology Conference: Society of Petroleum Engineers, 2012.

[12] Damjanac B, Cundall P. Application of distinct element methods to simulation of hydraulic fracturing in naturally fractured reservoirs. Computers and Geotechnics 2016;71(283-94.

[13] Watanabe N, Egawa M, Sakaguchi K, Ishibashi T, Tsuchiya N. Hydraulic fracturing and permeability enhancement in granite from subcritical/brittle to supercritical/ductile conditions. Geophysical Research Letters 2017;44(11):5468-75.

[14] Zhou J, Chen M, Jin Y, Zhang G-q. Analysis of fracture propagation behavior and fracture geometry using a tri-axial fracturing system in naturally fractured reservoirs. Int J Rock Mech Min 2008;45(7):1143-52.

[15] Ishida T, Aoyagi K, Niwa T, Chen Y, Murata S, Chen Q, et al. Acoustic emission monitoring of hydraulic fracturing laboratory experiment with supercritical and liquid CO2. Geophysical Research Letters 2012;39(16):n/a-n/a.

[16] Zoback MD, Rummel F, Jung R, Raleigh CB. Laboratory hydraulic fracturing experiments in intact and pre-fractured rock. International Journal of Rock Mechanics and Mining Sciences & Geomechanics Abstracts 1977;14(2):49-58.

[17] Ishida T, Chen Y, Bennour Z, Yamashita H, Inui S, Nagaya Y, et al. Features of CO2 fracturing deduced from acoustic emission and microscopy in laboratory experiments. Journal of Geophysical Research: Solid Earth 2016;121(11):8080-98.

[18] Zhou J, Jin Y, Chen M. Experimental investigation of hydraulic fracturing in random naturally fractured blocks. Int J Rock Mech Min 2010;47(7):1193-9.

[19] Zhou Z-L, Zhang G-Q, Xing Y-K, Fan Z-Y, Zhang X, Kasperczyk D. A Laboratory Study of Multiple Fracture Initiation from Perforation Clusters by Cyclic Pumping. Rock Mech Rock Eng 2018.

[20] Detournay E. Mechanics of Hydraulic Fractures. Annual Review of Fluid Mechanics 2016;48(1):311-39.

[21] Salimzadeh S, Usui T, Paluszny A, Zimmerman RW. Finite element simulations of interactions between multiple hydraulic fractures in a poroelastic rock. Int J Rock Mech Min 2017;99(9-20.

[22] Kumar D, Ghassemi A. Three-Dimensional Poroelastic Modeling of Multiple Hydraulic Fracture Propagation from Horizontal Wells. Int J Rock Mech Min 2018;105(192-209.

[23] Lu G, Gordeliy E, Prioul R, Aidagulov G, Bunger A. Modeling simultaneous initiation and propagation of multiple hydraulic fractures under subcritical conditions. Computers and Geotechnics 2018;104(196-206.

[24] Adachi J, Siebrits E, Peirce A, Desroches J. Computer simulation of hydraulic fractures. Int J Rock Mech Min 2007;44(5):739-57.

[25] Potyondy DO, Cundall PA. A bonded-particle model for rock. Int J Rock Mech Min 2004;41(8):1329-64.

[26] Lan H, Martin CD, Hu B. Effect of heterogeneity of brittle rock on micromechanical extensile behavior during compression loading. Journal of Geophysical Research: Solid Earth 2010;115(B1):B01202.

[27] Duan K, Kwok C. Evolution of stress‐induced borehole breakout in inherently anisotropic rock: Insights from discrete element modeling. Journal of Geophysical Research: Solid Earth 2016;121(4):2361-81.

[28] Scholtès L, Donzé F-V. A DEM model for soft and hard rocks: Role of grain interlocking on strength. Journal of the Mechanics and Physics of Solids 2012.

[29] Schöpfer MPJ, Childs C, Manzocchi T. Three-dimensional failure envelopes and the brittle-ductile transition. Journal of Geophysical Research: Solid Earth 2013;118(4):1378-92.

[30] Jain AK, Juanes R. Preferential Mode of gas invasion in sediments: Grain‐scale mechanistic model of coupled multiphase fluid flow and sediment mechanics. Journal of Geophysical Research: Solid Earth 2009;114(B8).

[31] Bruno MS. Micromechanics of stress-induced permeability anisotropy and damage in sedimentary rock. Mechanics of Materials 1994;18(1):31-48.

[32] Li L, Holt R. Particle scale reservoir mechanics. Oil & Gas Science and Technology 2002;57(5):525-38.

[33] Al‐Busaidi A, Hazzard J, Young R. Distinct element modeling of hydraulically fractured Lac du Bonnet granite. Journal of Geophysical Research: Solid Earth (1978–2012) 2005;110(B6).

[34] Duan K, Kwok CY, Wu W, Jing L. DEM modeling of hydraulic fracturing in permeable rock: influence of viscosity, injection rate and in situ states. Acta Geotech 2018.

[35] Shimizu H, Murata S, Ishida T. The distinct element analysis for hydraulic fracturing in hard rock considering fluid viscosity and particle size distribution. Int J Rock Mech Min 2011;48(5):712-27.

[36] Kwok C-Y, Duan K, Pierce M. Modeling hydraulic fracturing in jointed shale formation with the use of fully coupled discrete element method. Acta Geotech 2019.

[37] Raziperchikolaee S, Alvarado V, Yin S. Microscale modeling of fluid flow-geomechanics-seismicity: Relationship between permeability and seismic source response in deformed rock joints. Journal of Geophysical Research: Solid Earth 2014;119(9):6958-75.

[38] Yoon JS, Zimmermann G, Zang A, Stephansson O. Discrete element modeling of fluid injection–induced seismicity and activation of nearby fault. Canadian Geotechnical Journal 2015;52(10):1457-65.

[39] Hofmann H, Babadagli T, Yoon JS, Blöcher G, Zimmermann G. A hybrid discrete/finite element modeling study of complex hydraulic fracture development for enhanced geothermal systems (EGS) in granitic basements. Geothermics 2016;64(362-81.

[40] Hofmann H, Babadagli T, Yoon JS, Zimmermann G. Multi-branched growth of fractures in shales for effective reservoir contact: A particle based distinct element modeling study. Journal of Natural Gas Science and

Engineering 2016;35, Part A(509-21.

[41] Itasca. PFC2D Particle Flow Code in 2 Dimensions. 4.0 ed. Minneapolis2008.

[42] Zhao X, Young P. Numerical modeling of seismicity induced by fluid injection in naturally fractured reservoirs. Geophysics 2011;76(6):WC167-WC80.

[43] Sone H, Zoback MD. Mechanical properties of shale-gas reservoir rocks—Part 1: Static and dynamic elastic properties and anisotropy. Geophysics 2013;78(5):D381-D92.

[44] Ding W, Li C, Li C, Xu C, Jiu K, Zeng W, et al. Fracture development in shale and its relationship to gas accumulation. Geoscience Frontiers 2012;3(1):97-105.

[45] Fairhurst C, Hudson J. Draft ISRM suggested method for the complete stress-strain curve for intact rock in uniaxial compression. Int J Rock Mech Min 1999;36(3):279-89.

[46] Sneddon I. The distribution of stress in the neighbourhood of a crack in an elastic solid. Proceedings of the Royal Society of London Series A Mathematical and Physical Sciences 1946;187(1009):229-60.

[47] Goodfellow SD, Nasseri MHB, Maxwell SC, Young RP. Hydraulic fracture energy budget: Insights from the laboratory. Geophysical Research Letters 2015;42(9):3179-87.

[48] Anderson T. Fracture mechanics: fundamentals and applications. 4th ed: CRC Press, 2017.

[49] Kresse O, Weng X, Gu H, Wu R. Numerical Modeling of Hydraulic Fractures Interaction in Complex Naturally Fractured Formations. Rock Mech Rock Eng 2013;46(3):555-68.

[50] Duan K, Ji Y, Wu W, Kwok CY. Unloading-induced failure of brittle rock and implications for excavation-induced strain burst. Tunnelling and Underground Space Technology 2019;84(495-506.

[51] Potyondy D. A flat-jointed bonded-particle material for hard rock. 46th US Rock mechanics/geomechanics symposium: American Rock Mechanics Association, 2012.

[52] Gan Q, Elsworth D, Alpern JS, Marone C, Connolly P. Breakdown pressures due to infiltration and exclusion in finite length boreholes. Journal of Petroleum Science and Engineering 2015;127(329-37.

[53] Hubbert MK, Willis DG. Mechanics of Hydraulic Fracturing1. US Geological Survey 1957;210(153-68.

[54] Detournay E. Propagation Regimes of Fluid-Driven Fractures in Impermeable Rocks. International Journal of Geomechanics 2004;4(1):35-45.

Table 1. Micro-parameters used in the DEM model to simulate the propagation of simultaneously-induced multiple hydraulic fractures.

Particle property		Parallel bond property		Hydraulic property	
Property	Value	Property	Value	Property	Value
Particle density (kg/m^3)	3169	Parallel bond modulus (GPa)	23	Bulk modulus of fluid (GPa)	1
Young's modulus (GPa)	23	Parallel bond normal strength (MPa)	49±9.8	Fluid viscosity (Pa.s)	0.002
Friction coefficient	0.5	Parallel bond shear strength (MPa)	49±9.8	Pressure when the aperture decreases to half (MPa)	20
Minimum particle size, R_{min} (m)	0.752	Ratio between normal and shear stiffness	2.5	The residual aperture (m)	5×10^{-4}
Ratio between maximum and minimum particle size, R_{max}/R_{min}	1.66	Radius multiplier	1.0	Gap multiplier	1.0
Ratio between normal and shear stiffness, k_n/k_s	2.5				

Table 2. Comparison between the mechanical properties obtained from the experiments and the DEM simulations on the uniaxial compression test.

	Uniaxial compressive strength (MPa)	Young's modulus (GPa)	Poisson ratio
Experimental results	60.74	27.58	0.27
DEM results	60.46	27.39	0.25

Table 3 Setup of the DEM model and boundary condition for the simulation of simultaneous hydraulic fractures.

Model setup	Magnitude	Boundary condition	Magnitude
Width (m)	200	Initial pore pressure (MPa)	59.32
Height (m)	200	Horizontal stress (MPa)	70.26
Coordination number	4.09	Vertical stress (MPa)	82.74
Initial isotropic stress (MPa)	1.0	Loading rate when applying the in-situ stress (s^{-1})	0.0001
Number of parallel bonds	23529		

Table 4. States of the injection-induced single fracture at different stages. Stages A, C, and D are marked in Fig 7.

Stage	Injection time, t_{inj} (sec)	Coordinates of upper fracture tip		Coordinates of lower fracture tip		Coordinates of fracture center		Fracture length (m)	Half fracture length (m)
		x	*y*	*x*	*y*	*x*	*y*		
A	3275	3.09	3.66	-2.68	-10.71	0.2	-3.53	15.49	7.75
C	4011	3.09	6.59	-4.56	-28.53	-0.74	-10.97	35.94	17.97
D	7650	4.54	39.31	-4.56	-28.53	-0.01	5.39	68.45	34.23

Table 5. Cases designed to evaluate the influence of in-situ stress and pore pressure states on the interaction among multiple hydraulic fractures.

Case	Vertical stress, σ_V (MPa)	Maximum horizontal stress, σ_{Hmax} (MPa)	Initial pore pressure, P_0 (MPa)	Effective stress anisotropy ratio, α
Base case	82.74	70.26	59.32	2.14
Case I	82.74	65.00	59.32	4.12
Case II	82.74	75.00	59.32	1.49
Case III	75.66	70.26	59.32	1.49
Case IV	104.43	70.26	59.32	4.12
Case V	82.74	70.26	55.0	1.82
Case VI	82.74	70.26	65.0	3.37

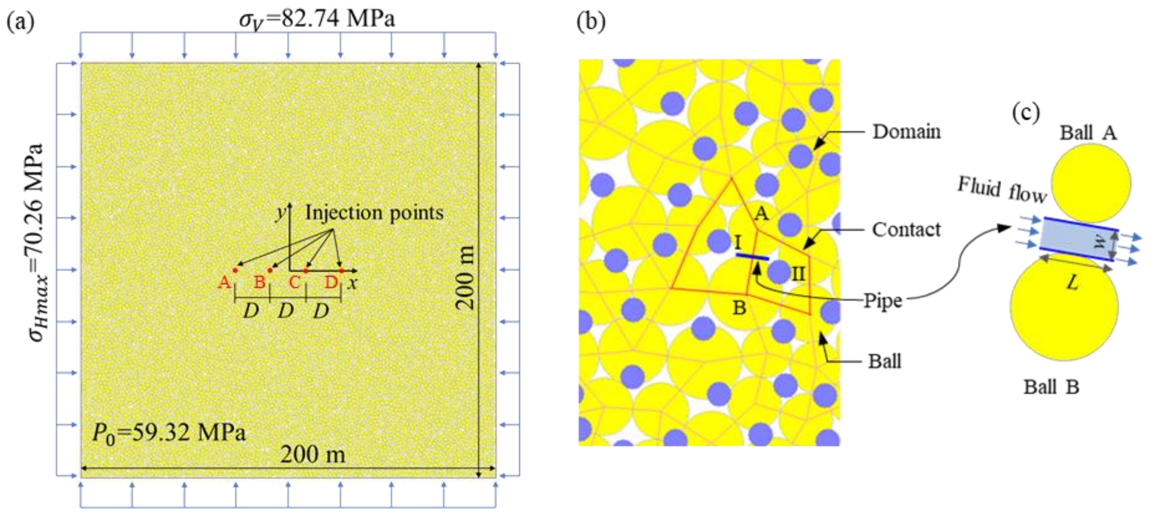

Figure 1. (a) Setup of the DEM model for the simulation of simultaneous multiple hydraulic fractures. The formation is saturated under the initial pore pressure P0=59.32 MPa. (b) Schematic diagram of the hydro-mechanical coupling model. (c) Idealization of fluid flow through the contact between two particles.

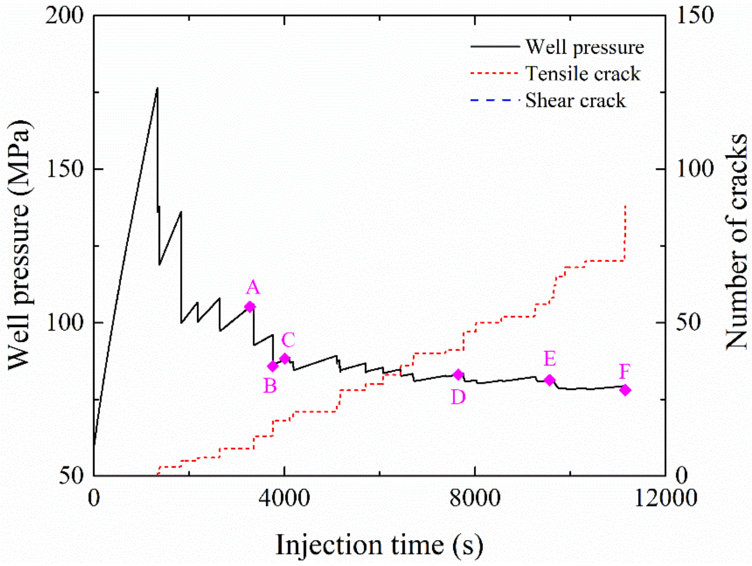

Figure 2. Well pressure history and the number of cracks from the single hydraulic fracturing treatment. Cracks are classified into tensile and shear modes according to their failure mechanism.

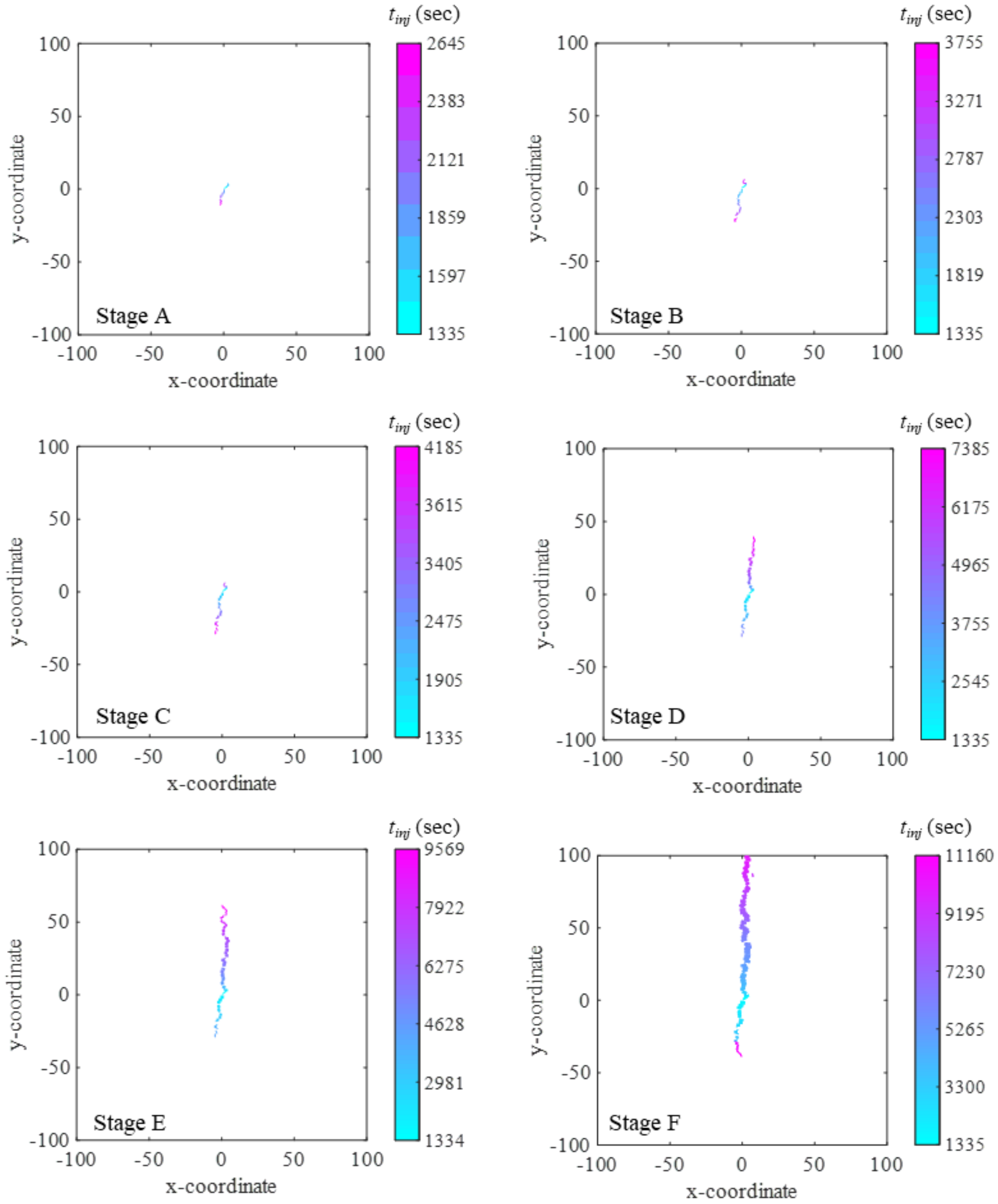

Figure 3. Growth of the single hydraulic fracture when injection is operated at the center of the formation. The thickness of the short line is proportional to the aperture of each crack, which are all formed as tensile failure. The aperture is normalized by 0.1 m. Corresponding stages are marked in the well pressure history in Fig 2.

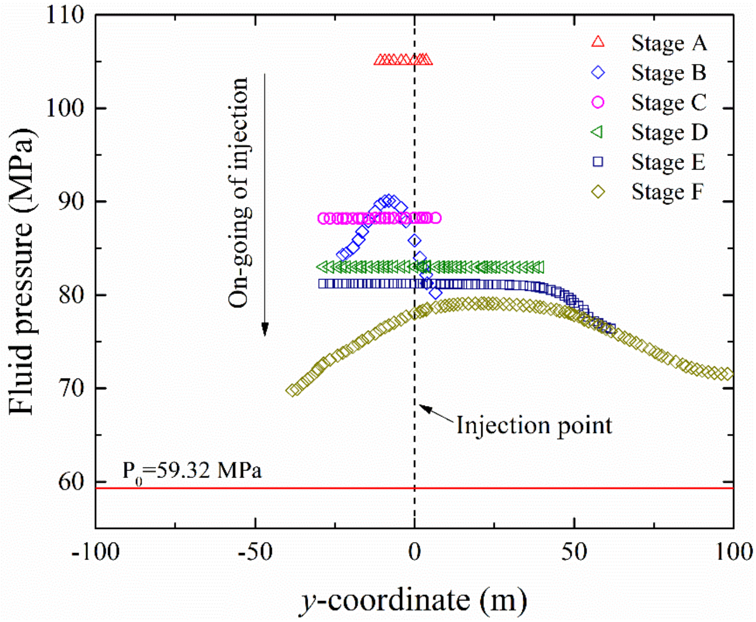

Figure 4. Distribution of the fluid pressure along the hydraulic fracture at various stages. Corresponding stages are marked in the well pressure history (Fig 2). The solid red line indicates the magnitude of initial pore pressure (P_0=59.32 MPa).

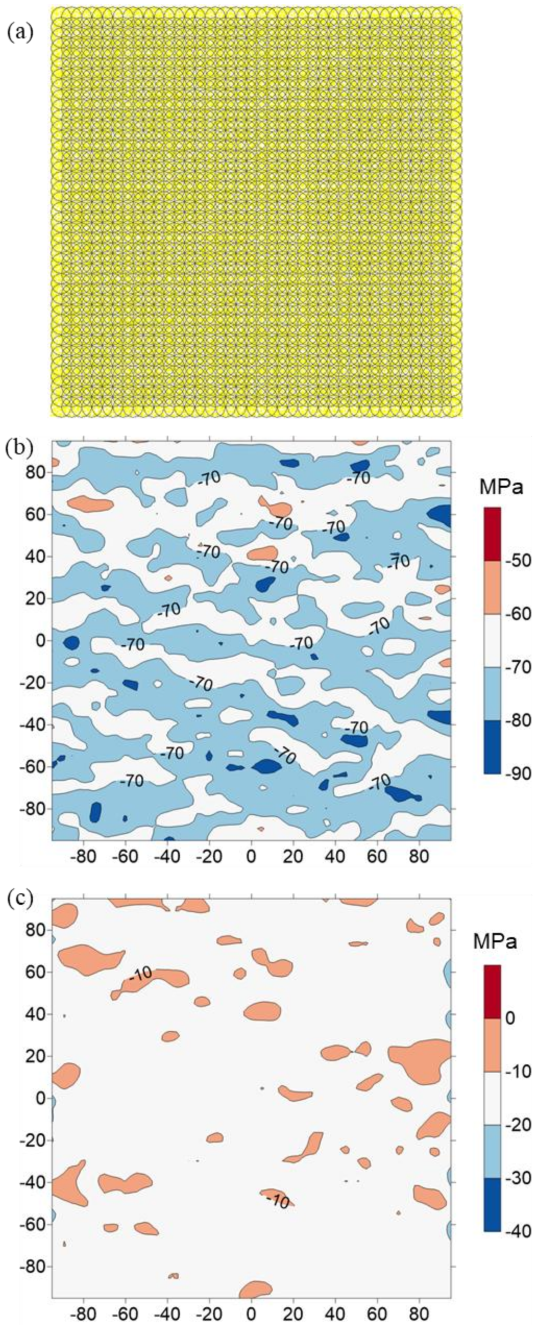

Figure 5. (a) Layout of the measurement circles. (b) Horizontal stress (σ_{xx}) measured after the application of in-situ stresses (σ_{Hmax}=70.26 MPa; σ_V=82.74 MPa); (c) Effective horizontal stress (σ_{xx}') measured after the formation is fully saturated under the initial pore pressure. Negative magnitude indicates the corresponding site is under compression.

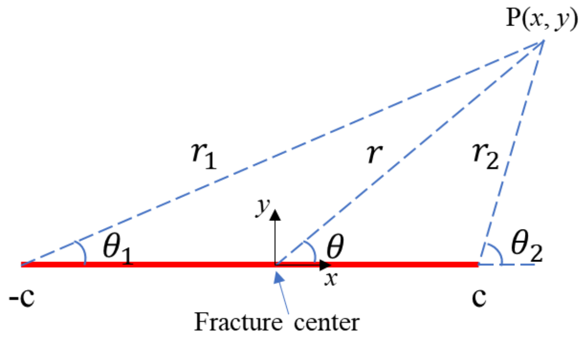

Figure 6. Schematic diagram of the model for the analytical solution (after *Sneddon* 1946). The pre-existing fracture is represented by the red solid line.

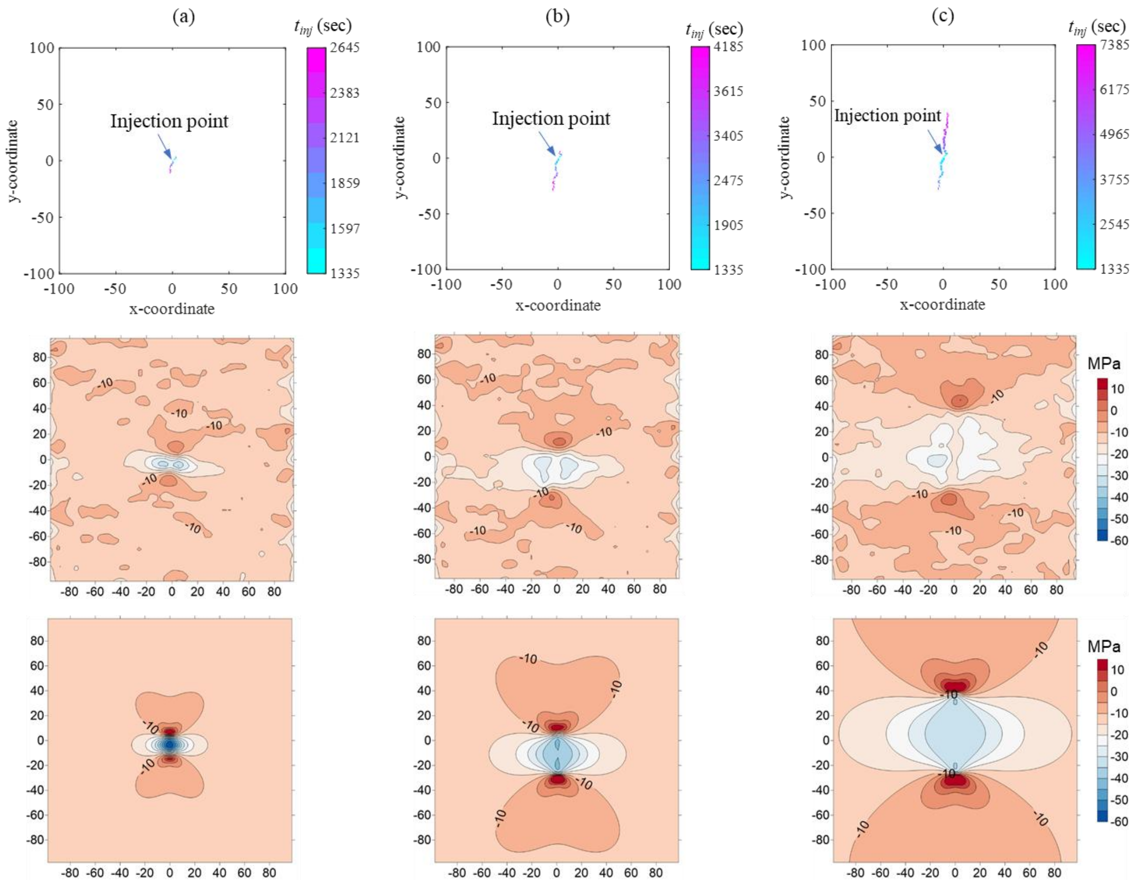

Figure 7. Induced cracks (top row), contour of $\sigma_{xx}{}'$ measured from the DEM model (middle row), and contour of $\sigma_{xx}{}'$ predicted by the analytical solution (bottom row). Three stages in Fig 2 are considered: (a) Stage A; (b) Stage C; and (c) Stage D.

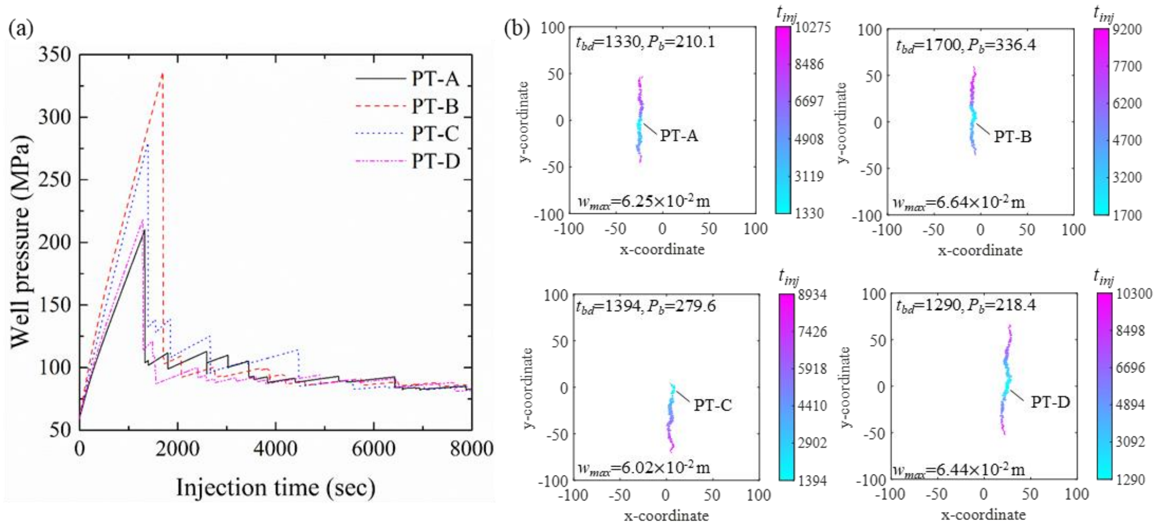

Figure 8. (a) Well pressure history from the four injection points when they are operated individually. (b) Geometry of the fractures in the end of the stimulation. Short lines represent the cracks. Color of the short lines indicates the formation time of fracturing. The thickness of the short line is proportional to the aperture of each crack. The maximum aperture (w_{max}), breakdown pressure time and magnitude are provided accordingly.

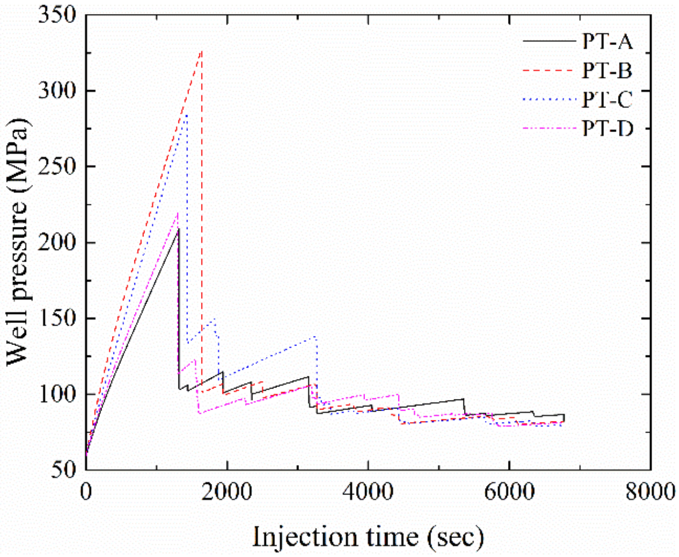

Figure 9. Well pressure histories from the simultaneous multiple hydraulic fracturing from a horizontal well. Spacing between adjacent injection points (D) equals to 17 m.

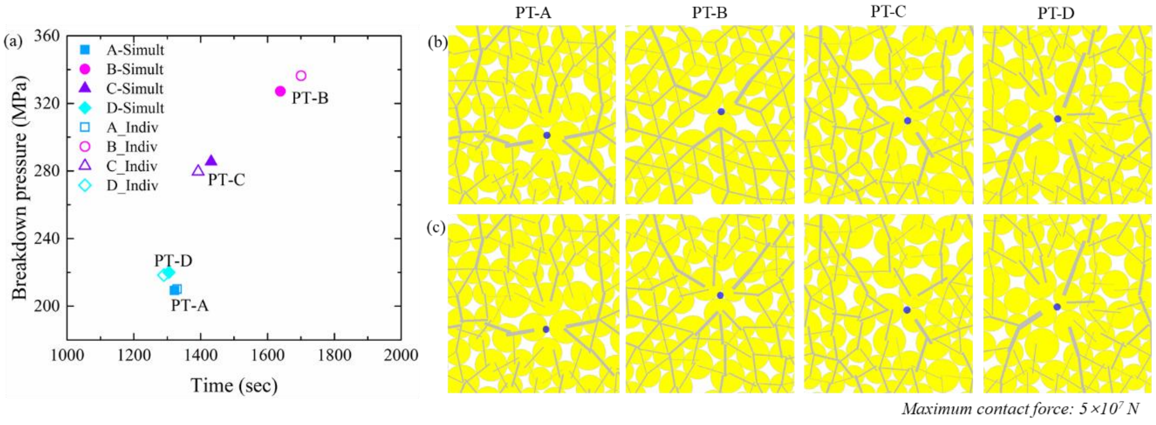

Figure 10. (a) Comparison of the breakdown pressure obtained from the simultaneous injection (solid symbols) and from individual injection tests (open symbols). (b) and (c) illustrate the contact force network around the injection point (blue dot) at the breakdown pressure stage obtained from the individual and simultaneous injection case, respectively. Thickness of the line is proportional to the magnitude of contact force.

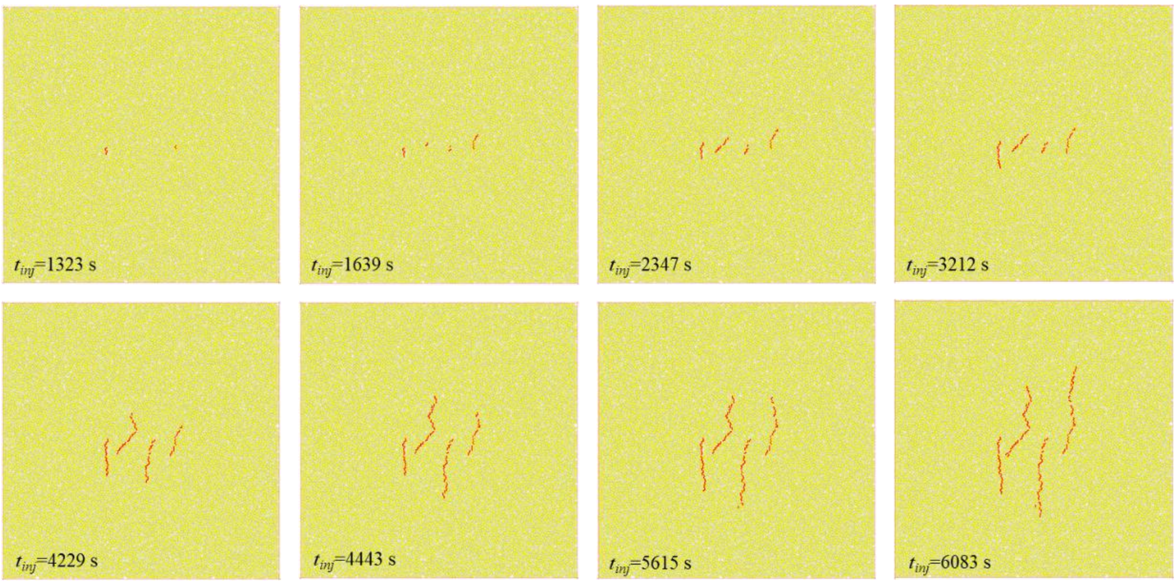

Figure 11. Initiation and propagation of the simultaneous multiple hydraulic fractures. Short red lines represent the cracks.

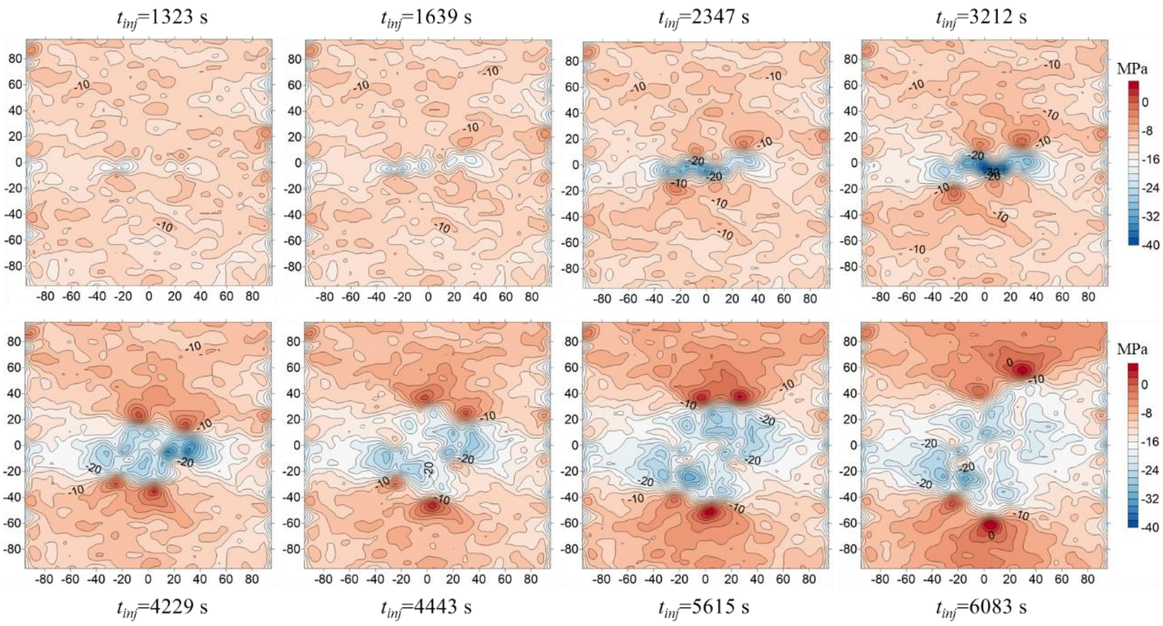

Figure 12. Contour of horizontal effective stress monitored from the DEM model at various stages during the growth of simultaneous multiple hydraulic fractures.

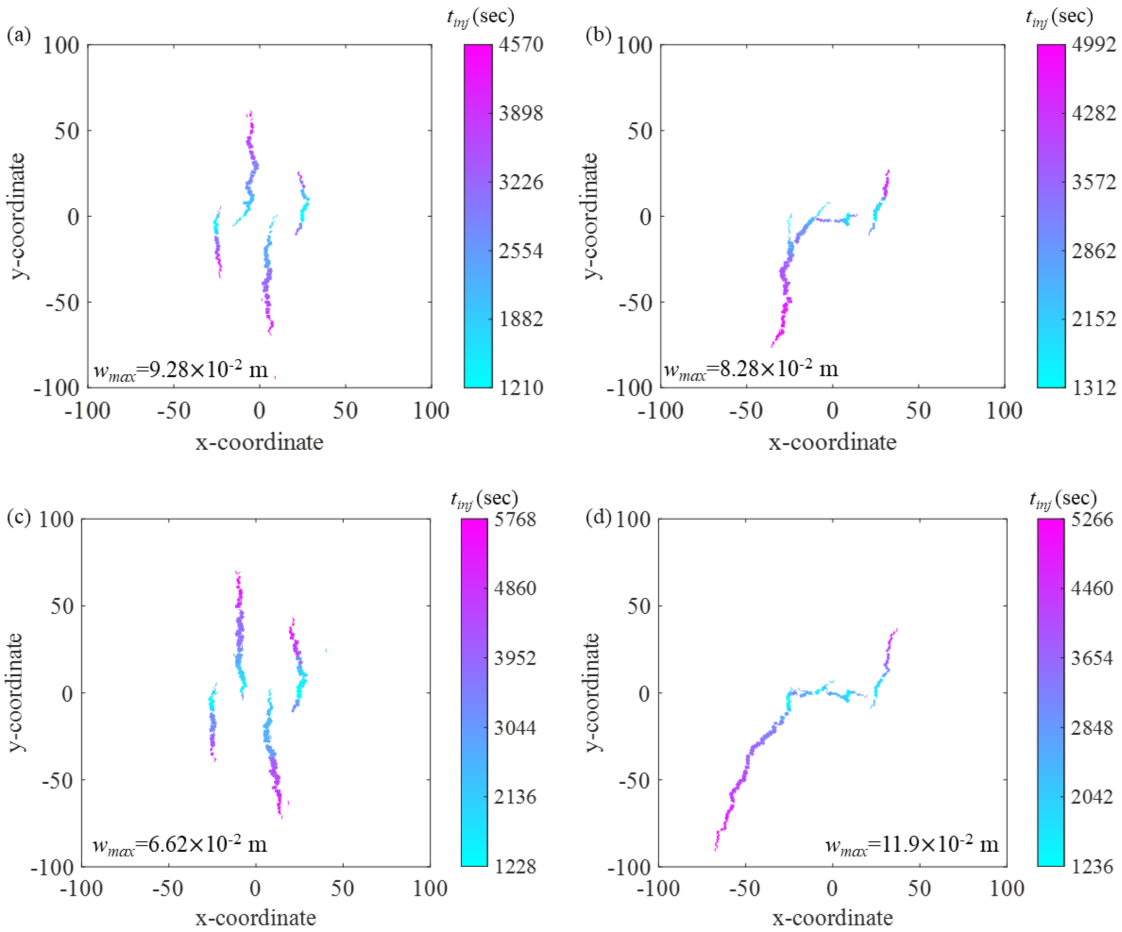

Figure 13. Influences of the in-situ stress anisotropy: (a) σ_{Hmax} =65 MPa, σ_V =82.74 MPa; (b) σ_{Hmax} =75 MPa, σ_V =82.74 MPa; (c) σ_{Hmax} =70.26 MPa, σ_V =104.43 MPa; and (d) σ_{Hmax} =70.26 MPa, σ_V =75.66 MPa. Short lines represent the cracks. Color of the short lines indicates the formation time of fracturing. The thickness of the short line is proportional to the aperture of each crack with the maximum magnitude (w_{max}) provided accordingly.

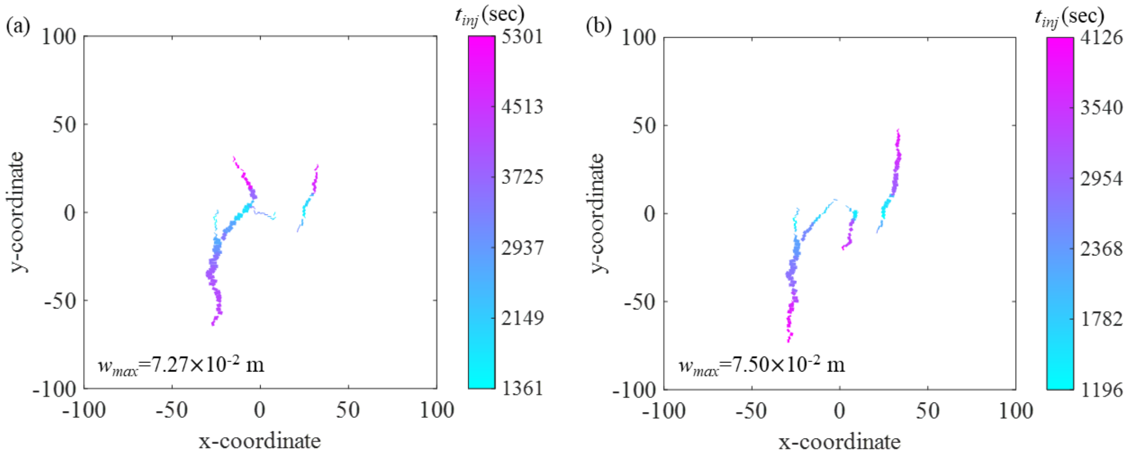

Figure 14. Influence of initial pore pressure (P_0): (a) P_0=55 MPa; (b) P_0=65 MPa. All other parameters are the same with the reference case. Short lines represent the cracks. Color of the short lines indicates the formation time of fracturing. The thickness of the short line is proportional to the aperture of each crack with the maximum magnitude (w_{max}) provided accordingly.

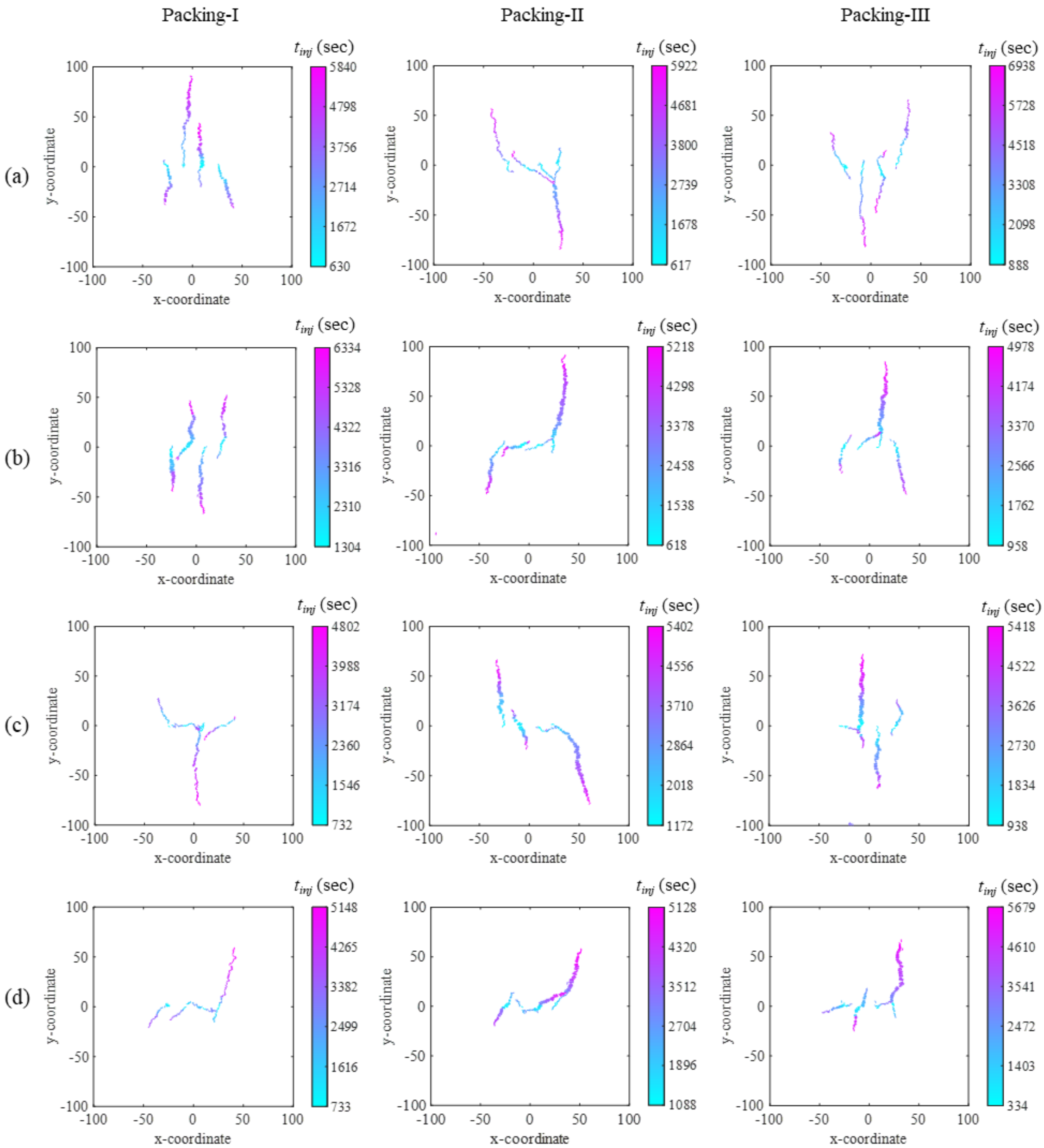

Figure 15. Influence of the formation heterogeneity. The particle size distribution is: (a) R_{max}/R_{min}=1.4, (b) R_{max}/R_{min} =1.66, (c) R_{max}/R_{min} =1.8 and (d) R_{max}/R_{min} =2.0. three packing modes are generated for each particle size distribution range. All other parameters are the same with the reference case. Short lines represent the cracks. Color of the short lines indicates the formation time of fracturing. The thickness of the short line is proportional to the aperture of each crack with the maximum magnitude (w_{max}) provided accordingly.

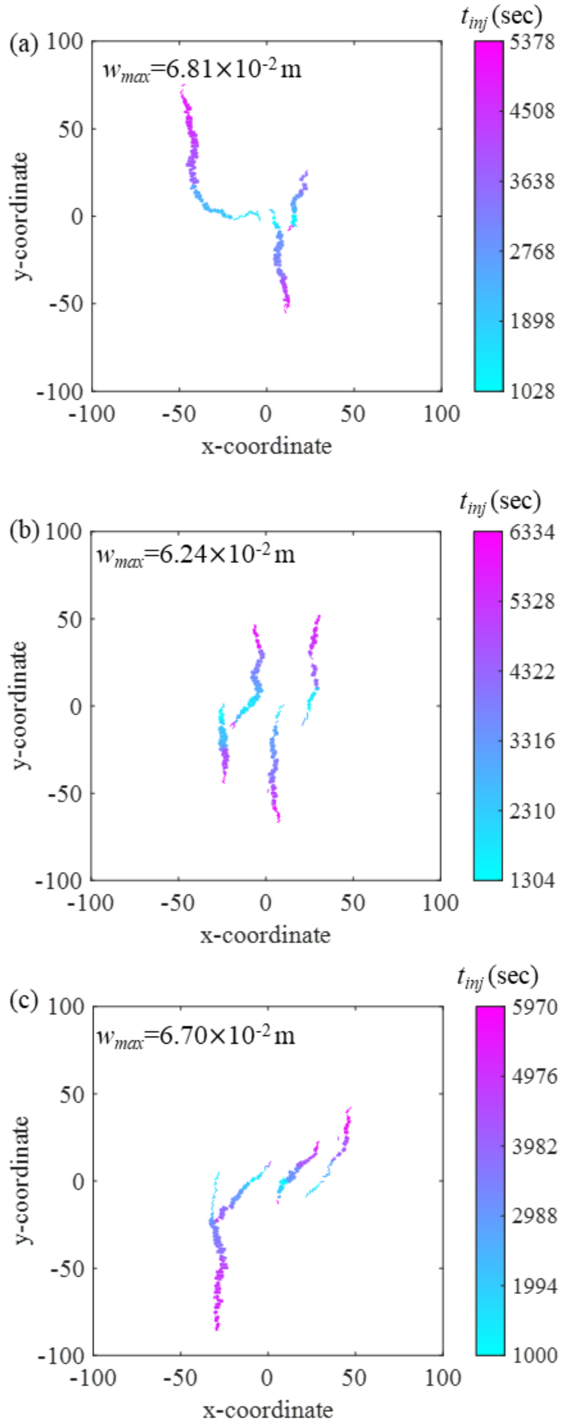

Figure 16. Influence of the spacing between injection points: (a) D=10 m, (b) D=17 m, and (c) D=20 m. All other parameters are the same with the reference case. Short lines represent the cracks. Color of the short lines indicates the formation time of fracturing. The thickness of the short line is proportional to the aperture of each crack with the maximum magnitude (w_{max}) provided accordingly.

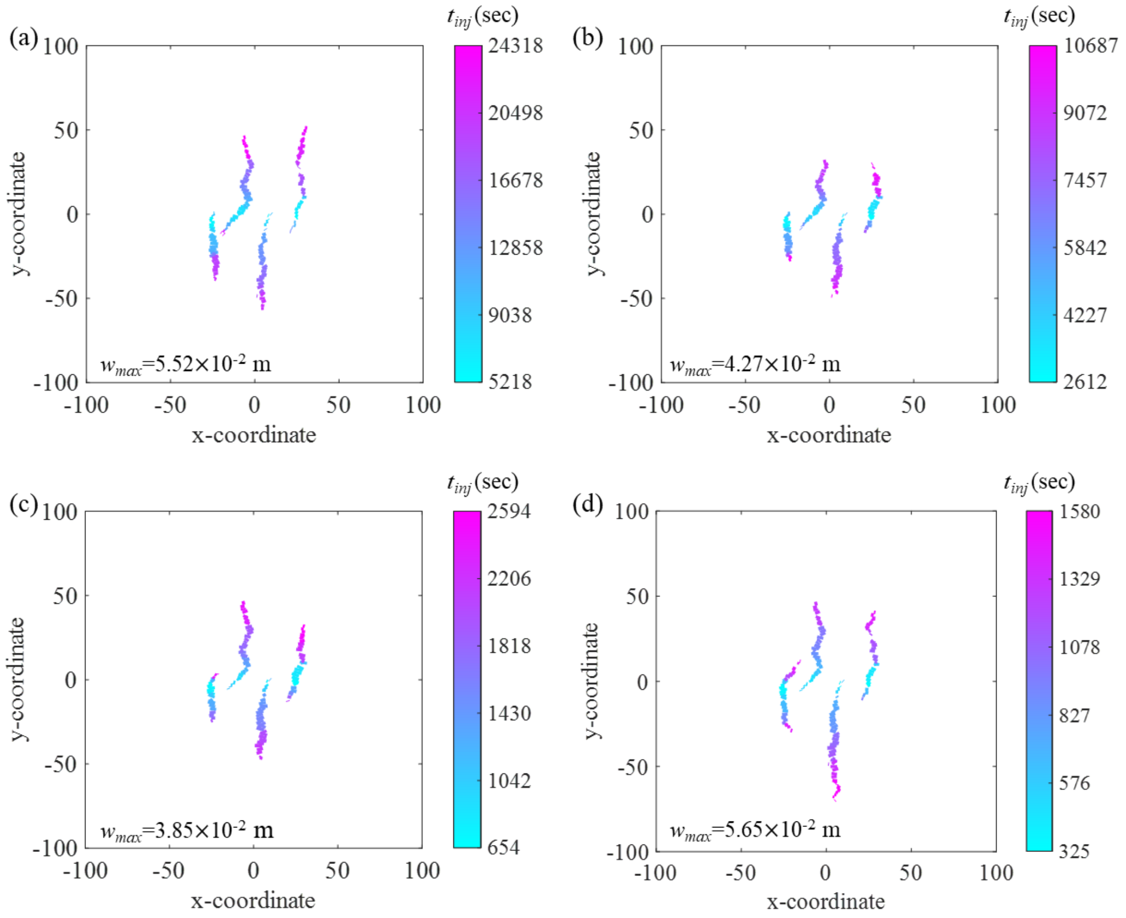

Figure 17. Influence of the injection rate. The injection rate equals to: (a) 1/4; (b) 1/2; (c) 2.0; and (d) 4.0 times of the reference case. Short lines represent the cracks. Color of the short lines indicates the formation time of fracturing. The thickness of the short line is proportional to the aperture of each crack with the maximum magnitude (w_{max}) provided accordingly.

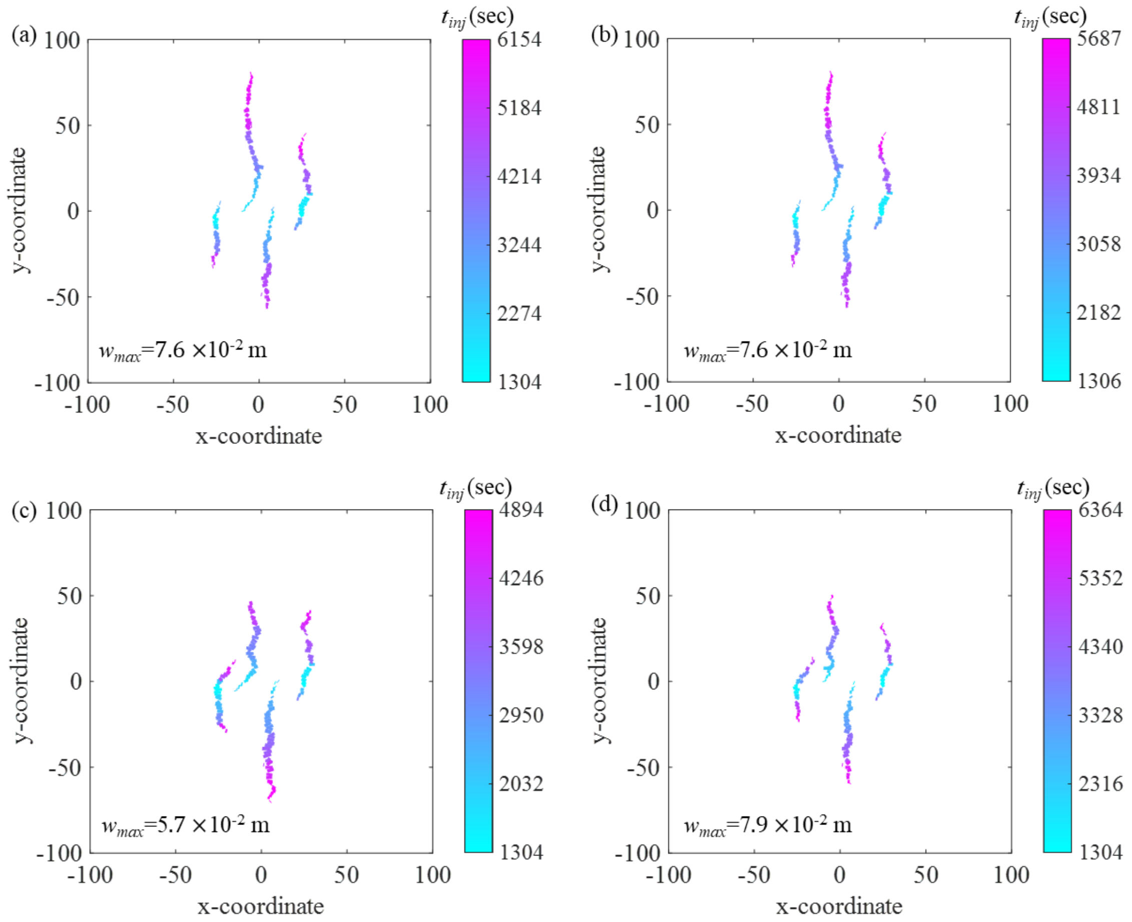

Figure 18. Influence of the fluid viscosity: (a) μ=0.0002 Pa.s; (b) μ=0.0005 Pa.s; (c) μ=0.005 Pa.s; (d) μ=0.02 Pa.s. All other parameters are the same with the reference case. Short lines represent the cracks. Color of the short lines indicates the formation time of fracturing. The thickness of the short line is proportional to the aperture of each crack with the maximum magnitude (w_{max}) provided accordingly.

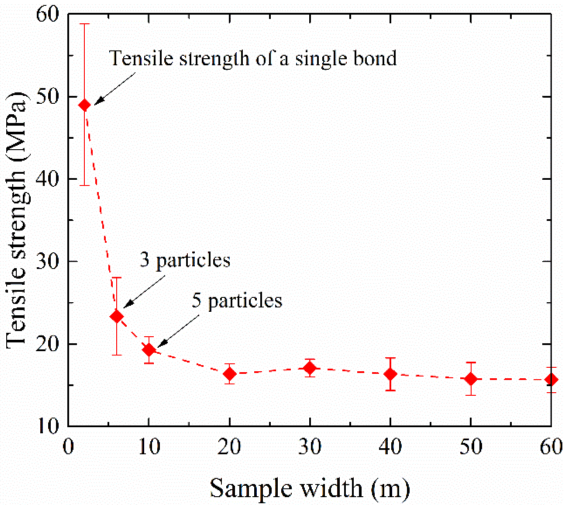

Figure 19. Tensile strength obtained from direct tensile tests on the DEM samples with various scales. For each scale, six samples were conducted by changing the random number. The ratio between height and width is kept constant as 2.0 for all the samples.